ISTITUTO NAZIONALE DI FISICA NUCLEARE

Sezione di Genova

INFN/BE-07/01
8 Giugno 2007

SOLENOID MAGNET AND FLUX RETURN FOR THE $\bar{\text{P}}$ANDA DETECTOR

Andrea Bersani[1], Renzo Parodi[1], Andrea Pastorino[1],
[1)] *INFN, Sezione di Genova, Dip. di Fisica, Univ. di Genova, I-16146 Genova, Italy*

Abstract

In this paper we present the project of the Solenoid Magnet for the PANDA detector developed in Genova. This project features a coil realized with a Rutherford–type, aluminum stabilized superconducting cable, wound inside an aluminum alloy coil former and indirectly cooled with a forced circulation of liquid helium. The concept of this magnet is based on many other working magnets, developed for different detectors, such as BaBar, Finuda, Delphi or CMS. A complete characterization of the magnetic, mechanical and thermal properties of the magnet is presented, with an ansatz on the time schedule to be followed to fulfill the detector deadlines.

PACS: 07.55.Db; 84.71.Ba; 29.30.-h; 29.30.Ep

Published by **SIS-Pubblicazioni**
Laboratori Nazionali di Frascati

The $\bar{\mathrm{P}}$ANDA[1] experiment is a 4π, high resolution spectrometer for low energy particle physics, mainly devoted to the study of QCD and related matters, using an antiproton beam colliding on an internal hydrogen target. The detector is formed by a barrel section, surrounding the interaction region, and a dipole section, used for the detection of the low-angle particles. We present a project of the solenoid for the barrel section: this project was developed to fulfill all the requirements coming from the detector people and was optimized in tight collaboration with the GSI technical experts. Even if the magnet concept is quite conventional, the geometrical constraints required a very important effort to be fulfilled simultaneously with the magnetic ones.

1 Physics Requirements and Performance Goals

The $\bar{\mathrm{P}}$ANDA target magnet is a thin, superconducting solenoid with an octagonal flux return yoke, as shown in fig. 1. Detector performance criteria and geometry considerations drive the design of the solenoid and the flux return. The magnitude and uniformity specifications for the magnetic field are derived from the tracker requirements: to achieve a mass resolution of the order of $10\,\mathrm{MeV}$ a magnetic field of $2\,\mathrm{T}$ is needed. The combined thickness of the vertex detector, outer tracker, particle identification system, electromagnetic calorimeter and appropriate clearences sets the cryostat inner diameter. The cryostat length is also constrained by the length of the nested subsystems and, critically, by the clearance requirements for the end cap detectors and for the servicing. The solenoid thickness has to be taken into account when evaluating the detection threshold of muons in the chambers hosted inside and outside the flux return yoke.

The shape of the downstream region of the yoke has been designed to allow the installation of several layers of muon chambers: a rough tracking of outgoing muons will be achieved thanks to this superlayer of steel and sensitive elements.

The minimum thickness in the barrel and in the end caps is calculated to avoid magnetic saturation and to stop pions: this is evaluated $\sim 40\,\mathrm{cm}$. End caps segmentation was studied to clamp the fringe fields without an eccessive increase of the amount of steel involved. Separation and movement of the end doors are constrained by beam line components, by the presence of the dipole magnet in downstream direction and by the need to provide ready access to detector subsystems.

The physics performance and operational requirements for the solenoid magnet and for the flux return (tables 1 and 2) are similar to those of many operating detector magnets.

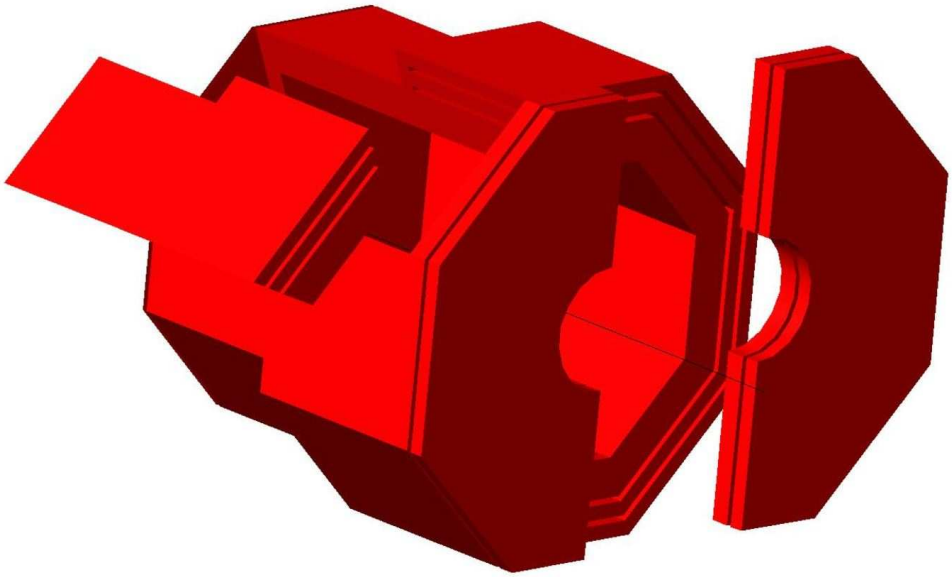

Figure 1: Iron yoke layout: in this picture, the front door is open and one sector is out from its work position for visualization.

2 Overview

The design of the superconducting coil for the $\bar{\mathrm{P}}$ANDA experiment is conservative and within the state of the art for detector magnets. It is based on the experience gained over the past 25 years with thin superconducting solenoids. Although specifically tailored to meet the requirements of $\bar{\mathrm{P}}$ANDA, this design is similar to many operating detector magnets. A common feature of all these magnets is the use of aluminum-stabilized conductors that are indirectly cooled by liquid helium pipes connected to an aluminum alloy support structure. This technique was first developed for CELLO[2], the first thin solenoid, and has been improved in subsequent designs. Table 2 shows the main features of some of these solenoid compared to the $\bar{\mathrm{P}}$ANDA design. All these designs used a Rutherford-type cable made of NbTi superconductor encased in an aluminum stabilizer that allows for adequate quench protection.

The $\bar{\mathrm{P}}$ANDA detector schedule identifies the magnet as a critical procurement item: the setup of the yoke, cryostat and solenoid is compulsory for the installation of all the ac-

Solenoid Requirements	
Central induction	$2\,\mathrm{T}$
Uniformity in outer tracker	$\pm 2\%$
Nuclear interaction length	$0.4\lambda_{int}$
Cryostat inner radius	$950\,\mathrm{mm}$
Cryostat outer radius	$1340\,\mathrm{mm}$
Minimization of thermal cycling	

Flux return Requirements
Provide an external path for the magnetic field
Provide support and stopping for muon chambers
Provide gravitational load for the detector
Movable end doors to allow access inside the barrel

Table 1: Physics performances and operational requirements for the $\bar{\mathrm{P}}\mathrm{ANDA}$ solenoid.

tive parts of the detector. This is due to the fact that the cryostat itself provides mechanical support for the various detectors: so, before the assembly, also tests and commissioning of the magnet are needed. The solenoid design, fabrication and commissioning duration foreseen is $30 \div 36$ months, so the contract should be awarded in the summer of 2008 to meet the overall detector schedule.

The magnet cryostat will be designed, fabricated and inspected according to the intent of the ASME Boiler and Pressure-Vessel Code, Section VIII, Division 2 [3], but will not be code-stamped. For steel structures, the allowable design stresses follow the standard guidelines of European and Italian standards [4][5]. Bolted connections and fasteners will conform to their recommended torques and allowable stresses depending on the connection. The flux return is fabricated with S235 JR structural steel plates or a material with similar mechanical and magnetic properties.

2.1 Descritpion of Key interfaces

Superconducting Solenoid and Flux Return.

The radial distance between the outer diameter of the cryostat and the inner surface of the barrel flux return is $100\,\mathrm{mm}$: in this space is foreseen a double layer of muon detectors. The presence of muon chambers inside the barrel is compulsory to achieve a sufficient tracking capability for low energy muons. The solenoid weigth and magnetic forces are transmitted to the yoke by means of titanium and structural steel supports. These attachments, providing also the load path for the inner detector components to the

	ZEUS	ALEPH	BABAR	PANDA
Location	DESY	CERN	SLAC	GSI
Manufacturer	Ansaldo	Saclay	Ansaldo	?
Year completed	1988	1986	1997	2010?
Central field (T)	1.8	1.5	1.5	2
Inner bore (m)	1.85	4.96	2.8	1.9
Length (m)	2.5	7	3.46	2.7
Energy (MJ)	12.5	137	25	20
Current (A)	5000	5000	7110	5000
Weigth (t)	2.5	60	6.5	5?
Rad. length	0.9	1.6	1.4	0.5?
Cable section (mm)	4.3×15	3.6×35	3.2×30	3.3×25
Current density ($\frac{\mathrm{A}}{\mathrm{mm}^2}$)	78	40	74	50

Table 2: Comparison of solenoids used in experiments similar to $\bar{\mathrm{P}}\mathrm{ANDA}$.

barrel flux return, are described in detail in the next sections.

In the barrel are foreseen different chases for the cryostat chimney and for the target pipe: these chases have proper shapes and dimensions of the order of $20 \div 50\,\mathrm{cm}$. The signal cables exit through the upward end doors and through attidional rectangular chases between the barrel and the doors.

Barrel and End Doors.

Both end doors have $\sim 90\%$ solid steel contact area at the surface with the ends of the barrel. The remaining 10% area of the barrel ends is reserved for cabling and utilities from the inner detector components. The end doors are attached to the barrel with tie plates that are bolted to the end door structure and to the barrel itself.

Particle Identification System.

The Particle Identification is obtained mainly thanks to a DIRC whose silica stakcs are placed between the tracker and the calorimeter. The Čerenkov light produced in the DIRC has to be projected on an array of small PMTs in order to measure the radius of the Čerenkov cone and to reconstruct the particle speed. This PMTs have to be placed outside the yoke in a region with magnetic field less than $10\,\mathrm{G}$. On the other hand, the lenght of the stacks has to be minimized to reduce light loss and costs. A magnetic shield made of iron and mu–metal is foreseen to achieve the desired field in PMTs region: the suspension system for the DIRC water vessel and for this shield is not defined yet.

Inner Muon Detector and Solenoid.

There is a muon counter between the cryostat and the yoke. This detector is directly

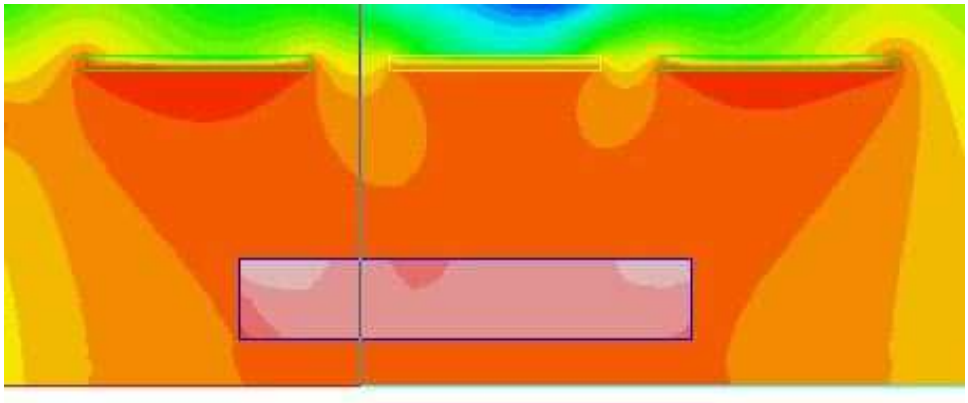

Figure 2: Field uniformity inside the solenoid: in pink the outer tracker region (division is 1%).

attached to the barrel, and, with the microvertex detector, which is suspended to the beam pipe, is the only one that doesn't load the cryostat. Because of the presence of the cryostat support, a proper design for the muon plates located inside the barrel is needed.

Movable End Door Skids and the Beam Line.

The end doors are mounted on skids equipped with rollers so that they can be moved away from the barrel for maintenance access. The end door skids move on tracks installed in the floor. The end doors clear the beam line magnets, vacuum pumps, magnet stands, and other beam line equipment during door opening.

External Platforms, Stairways, and Walkways.

The external platforms necessary to install and service electronic racks and cryogenic equipment are supported from the flux return. The requirements of these components have not yet been determined.

3 Summary of Projected Magnet Performance.

3.1 Central Field Magnitude and Coil Performance.

The magnetic field of $2\,\mathrm{T}$ is obtained by energizing the solenoid with a constant current of $5000\,\mathrm{A}$. The conductor is operated at 50% of the critical current, with a peak field in the conductor of $2.8\,\mathrm{T}$. This gives a large safety margin.

Magnetic uniformity is achieved by using different current densities in regions at both ends of the solenoid w.r.t. the central region. This is done by adding more aluminum

stabilizer to the central region conductor, which reduces the current density there. Fig. 2 shows the field uniformity in the central region. The areas in which the field nonuniformity is greater than 1.5% are small and are located in regions in which they do not affect the performance of the drift chamber. In addition, once the solenoid parameters are optimized, the corners of the drift chamber are also within $\pm 2\%$ of $2\,\mathrm{T}$.

The radial pressure due to magnetic forces on the conductor during operation is $\sim 2.90\,\mathrm{MPa}$ in the high current density regions and $\sim 1\,\mathrm{MPa}$ in the central region of the conductor. An aluminum alloy support cylinder surrounds the coiled conductor to react against these radial pressures and keep the conductor from yielding.

The integrated axial force on the winding is $\sim 8\,\mathrm{MN}$. The conductor winding and support cylinder are mechanically coupled by an epoxy bond. This epoxy bond allows some of the axial load to be transmitted in shear to the outer aluminum cylinder, which keeps the conductor from yielding. There is an axial $\sim 1\,\mathrm{MN}$ decentering force applied to the conductor winding due to the asymmetry in the iron yoke.

3.2 Flux Return

The flux return assembly provides an external flux path for the magnetic field of the superconducting solenoid. Fig. 3 shows the flux lines from the magnetic analysis. There are large body forces acting on the coils and on the end doors as a result of the magnetic field.

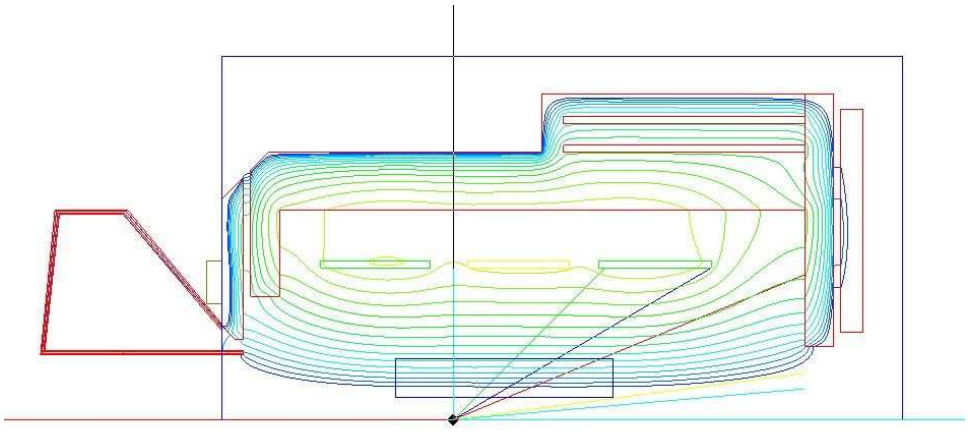

Figure 3: Flux lines all over the detector.

4 Superconducting Solenoid

4.1 Magnetic Design

This section describes the main features of the superconducting solenoid. A cross section of the solenoid is shown in fig. 4, and parameters are given in table 3.

The magnetic analysis is based on a two–dimensional axially symmetric model and on a complete three–dimensional model. These models include the solenoid, flux return yoke, shields, some ancillary equipments and end doors.

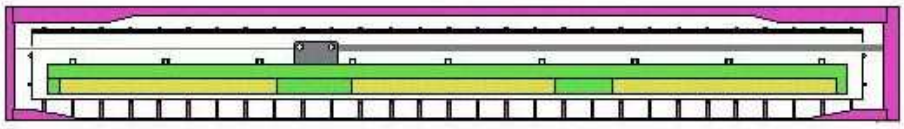

Figure 4: Coil schematics: in purple the cryostat, in green the coil former, in yellow the windings.

The backward shield is designed to accommodate the DIRC. Its main functions are to improve the field uniformity in the backward region of the outer tracker and to balance the magnetic force on the solenoid due to the yoke asymmetry. A detailed design of this shield is underway. The iron properties used for computation ([6] two–dimensional magnetic element) are those of hot–rolled carbon steel.

The magnet design provides a magnetic field of $2\,\mathrm{T}$ with a uniformity of $\pm 2\%$ in the tracking region. This is obtained by grading the current density of the solenoid in three regions connected in series. The central region is $700\,\mathrm{mm}$ in length with 133 turns. Two end regions are $755\,\mathrm{mm}$ and $780\,\mathrm{mm}$ in length with 216 and 223 turns respectively. The current density in the end regions is 1.5 times that of the central part. A better field uniformity may be obtained by reducing the axial length of the two end regions and increasing the current to generate the same field, but this would cause a reduction in stability against thermal disturbance. For the initial design, the maximum allowed current density in the conductor has been limited to the maximum currently attainable for magnets of this kind, i.e., $80\,\mathrm{A/mm^2}$ (ZEUS magnet). In these conditions, a cross section of $80\,\mathrm{mm^2}$ for the smaller conductor corresponds to a maximum current of $\sim 6400\,\mathrm{A}$: our choice of $5000\,\mathrm{A}$ gives a good margin for operations.

Fig. 5 shows the graph of the field strength over the full detector region. The

Parameter	Value
Central Induction	$2\,\mathrm{T}$
Conductor Peak Field	$2.8\,\mathrm{T}$
Uniformity in the Tracking Region	$\pm 2\%$
Winding Length	$2.7\,\mathrm{m}$
Winding Mean Radius	$1070\,\mathrm{mm}$
Amp Turns	$5.86 \cdot 10^6$
Operating Current	$5000\,\mathrm{A}$
Inductance	$1.6\,\mathrm{H}$
Stored Energy	$20\,\mathrm{MJ}$
Total Length of Conductor	$8000\,\mathrm{m}$

Table 3: The main parameters of the winding of the $\bar{\mathrm{P}}\mathrm{ANDA}$ solenoid.

magnetic field is essentially symmetric: in addition, a field uniformity better than $\pm 2\%$ is obtained in the inner and outer tracker regions. Field uniformity is required up to $z = 1100\,\mathrm{mm}$ in the forward region, and the present design provides a uniform field up to $z = 1200\,\mathrm{mm}$, providing a factor of safety. Further adjustment of the backward shield geometry may improve field quality, in the sense of an improvement of the field uniformity in the backward region.

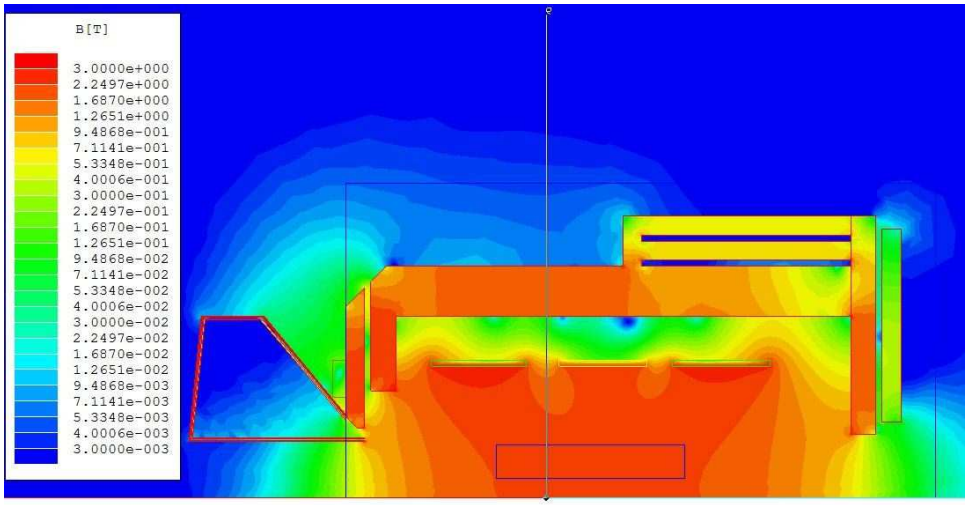

Figure 5: The field strength over the full detector region.

4.2 Cold Mass Design

Aluminum Stabilized Conductor

The conductor is composed of a superconducting Rutherford cable embedded in a very pure aluminum matrix by a coextrusion process that ensures a good bond between aluminum and superconductor. Table 4 shows the main parameters of the conductor.

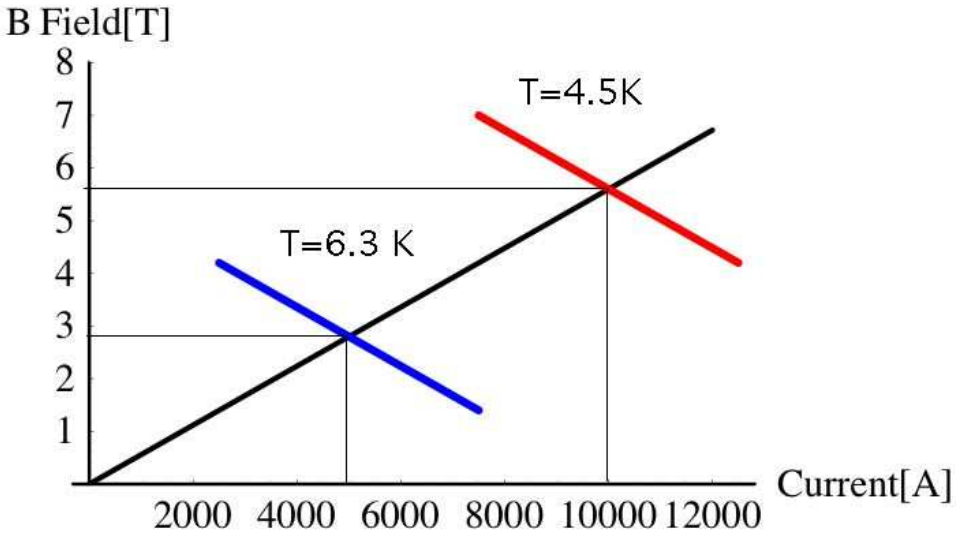

Figure 6: Superconducting cable work point calculation. The red line represents the current sharing vs. magnetic field curve at $4.5\,\mathrm{K}$ calculated for our cable: the cable was chosen to be critical at twice the current and twice the magnetic field w.r.t. he work ones. The blue line represents the sharing current vs. magnetic field at the work condition ($I = 5000\,\mathrm{A}$, $B = 2.8\,\mathrm{T}$): the sharing current temperature is here $6.3\,\mathrm{K}$, giving us a safety margin $\Delta T = 1.8\,\mathrm{K}$.

The operating current for this conductor is 50% of the critical current at twice the peak field, giving a large safety margin. In the case of local heating up to $5.2\,\mathrm{K}$, there is still a significant margin on the critical current ($I = 0.6 I_c$). At $2.8\,\mathrm{T}$, the conductor critical temperature is $T_c = 8.15\,\mathrm{K}$, and the current sharing temperature is $6.3\,\mathrm{K}$. This values can be calculated using the Lubell Formulas[7]:

$$T_c(B) = 9.25\,\mathrm{K}\left(1 - \frac{\mathrm{B[\,T]}}{14.5\,\mathrm{T}}\right)^{0.59} \tag{1}$$

which describes the critical temperature as a function of the magnetic field on the con-

ductor and

$$J_c(B) = J_0 \left(1 - \frac{T}{T_c(B)}\right) \tag{2}$$

which describes the critical current density as a function of the magnetic field on the conductor and of the temperature.

A simple method to evaluate the stability of the winding consists of considering the enthalpy margin per unit length between the operating and the sharing temperature. This stability parameter for the $\bar{\mathrm{P}}\mathrm{ANDA}$ solenoid is $0.5\,\mathrm{J/m}$, which is the same value obtained for the ALEPH and BaBar magnets.

The cross section of the conductor is $3.3 \times 24.6\,\mathrm{mm}^2$ for the higher current density regions and $5.15 \times 24.6\,\mathrm{mm}^2$ for the central region. The coil winding can be made using six $1500\,\mathrm{m}$ lengths of conductor, requiring five electrical joints. Each joint, made by either by TIG welding (as in the Atlas barrel Toroid and CMS), or soft soldering (after electro–deposition of copper) a suitable length of the aluminum matrix must have a resistance less than $5 \cdot 10^{-10}\Omega$, limiting the power dissipation to a few milliwatts.

Winding Support

The winding will be supported by an external aluminum alloy cylinder similar to other existing detector magnets. The winding support is designed for all aspects of force containment, i.e., its weight and the radial and axial magnetic forces. Fig. 7 shows these magnetic forces on the solenoid.

The maximum radial pressure, $\sim 2.90\,\mathrm{MPa}$, is generated in the high current density regions at the ends of the coils. A pressure of $\sim 1\,\mathrm{MPa}$ is generated in the central region. An aluminum alloy (Al 5083 T0) support cylinder surrounds the coiled conductor to react against these radial pressures and prevent coil movement. An extended stress analysis of the solenoid coil-support cylinder assembly has been developed to investigate the behaviour of the high-ductility pure aluminium stabilizer and epoxy resin under the high radial pressures generated by magnetic forces. The cable was thus simulated including the material non-linear stress-strain curve. As a result, plastic deformations are expected to occur in the coils during the first charge. The amount of these deformations is small and ensures that the cable will not be stressed beyond the elastic limit in the subsequent charges. This will help prevent premature quenching during coil energizing. Nevertheless, the support cylinder is capable to contain the deformations of the coils while remaining in the elastic field.

An integrated compressive axial force of $\sim 8\,\mathrm{MN}$ is induced in the winding. The distribution of the axial force within the coil is complex. The central part is slightly axially stressed by a force of less than $1\,\mathrm{MN}$. For preliminary calculations of the axial stress, the maximum force was considered ($4.3\,\mathrm{MN}$ in the worst case for one of the three

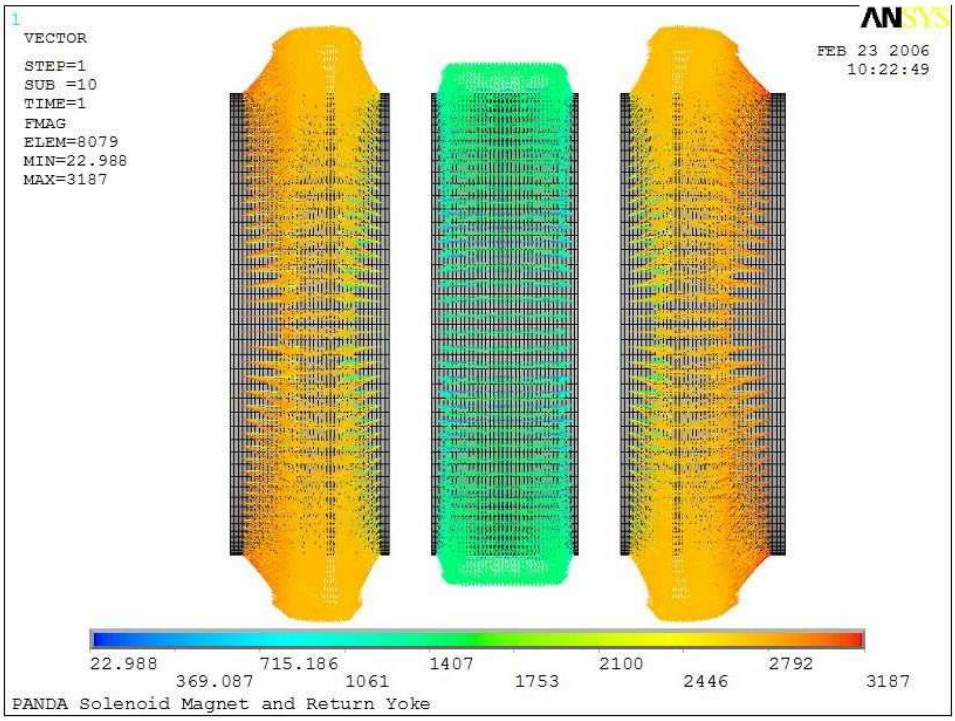

Figure 7: The force distribution on the coils (beam direcion is left–to–right).

coils). This would lead to an axial stress of $13\,\mathrm{MPa}$ on the pure aluminum, with only the winding supporting the axial forces. However, if the axial force is transmitted to the outer cylinder, the stress is considerably lowered. In this case, the shear stress between the winding and outer supporting cylinder is less than $3\,\mathrm{MPa}$. This low value of shear stress will allow the winding and support cylinder to be mechanically coupled through an epoxy impregnation without applying any axial prestress to the winding (as was done for the ZEUS and BaBar magnets). Epoxy impregnation can support a shear stress higher than $30\,\mathrm{MPa}$, providing a high safety margin. This leads to a simplification and cost saving in the winding fabrication.

The current design causes axial decentering forces on the coil due to the iron asymmetry and a residual force of $1\,\mathrm{MN}$ is applied to the winding. A more careful design of the backward shield can help reduce the amount of this residual axial force by some 10%: nevertheless, this force has to be supported by specifically designed and calculated structures. For this purpose, 8 axial bars, made of high-resistance Titanium alloy, have been foreseen, together with 16 radial bars, which account for the weight of the barrel and possible forces due to a misalignment of the assembly with respect to the central axis.

Parameter	Value
Conductor Type	NbTi Pure Al–stabilized Co–extruded
Aluminum RRR	> 500
Conductor Unit Length	$1.5\,\mathrm{km}$
Number of Lengths	6
Bare dimensions	3.3 and $5.15 \times 24.6\,\mathrm{mm}^2$
Insulated dimensions	3.7 and $5.55 \times 25\,\mathrm{mm}^2$
Superconducting Cable	Rutherford type
Dimensions	$9 \times 1.23\,\mathrm{mm}^2$
Strands Diameter	$0.84\,\mathrm{mm}$
Number of Strands	20
Cu/Sc	1.8
Filament Diameter	$20\,\mu\mathrm{m}$
$I_c(B = 2.5\,\mathrm{T},\ \mathrm{T} = 4.5\,\mathrm{K})$	$> 10\,\mathrm{kA}$
Insulation Type	Fiberglass Tape
Insulation Thickness	$0.4\,\mathrm{mm}$

Table 4: Conductor parameters.

While the preliminary analyses described above decoupled the effects of radial and axial magnetic forces on the coils and support cylinder, a comprehensive 3D FEM analysis has been made simulating the coil and cylinder assembly under the effect of the magnetic field during nominal operations. The results of this calculation (see Fig. 8), confirming previous analyses, are pointed out below:

- The radial pressure generated in the windings causes the pure aluminium stabilizer to exceed its elastic limit, showing permanent deformations after the first charge. Nevertheless, the amount of the plastic deformations is negligible and stresses will remain within the elastic range during the subsequent charges.

- The shear stress transmitted through the epoxy resin to the aluminium support cylinder is fairly low if compared to the resin capabilities.

- Stability of the whole assembly is ensured by the Al 5083 aluminium barrel. The analysis show that the cylinder is capable to contain the radial and axial deformations of the windings without showing permanent deformations.

- Axial and radial supports have also been included in the model. The decentering

forces caused by the asymmetry of the return flux and the weight of the assembly are well supported by the suspension system, the stresses calculated for the bars being well below the elastic limit for Titanium alloys (Ti 6Al 4V or Ti 5Al 2.5Sn).

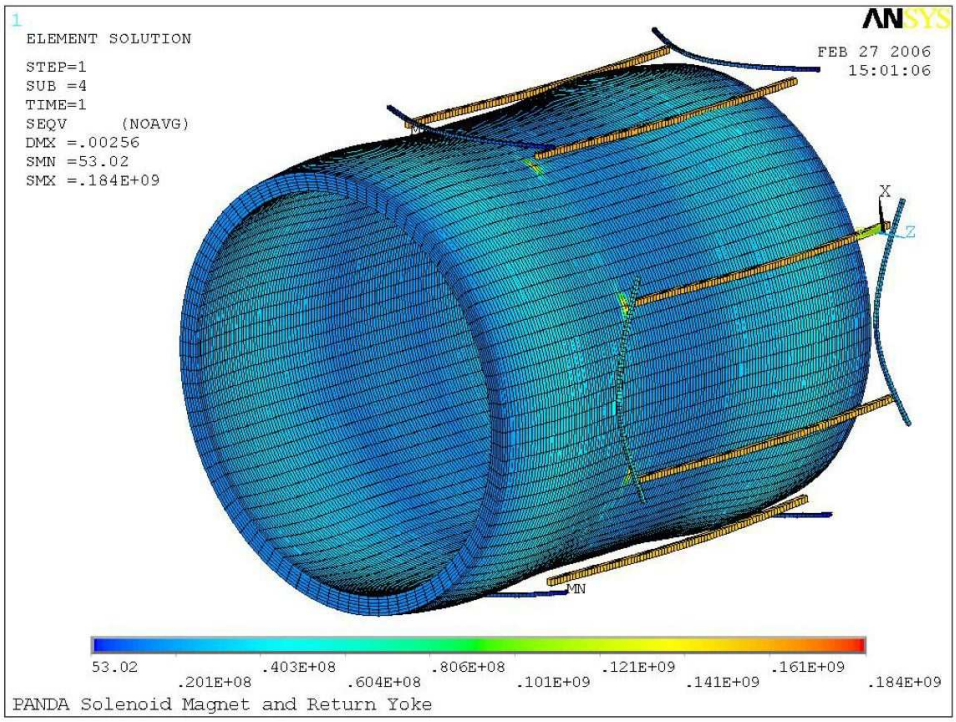

Figure 8: Stress on solenoid coil, barrel and supports.

Table 5 shows the main features of the cold mass. The values are given at a temperature of $4.2\,\mathrm{K}$. The dimensions at room temperature are higher by a factor of approximately 1.004.

Electrical Insulation

Electrical insulation is an important aspect of solenoid design and manufacture. Two categories of insulation are required: ground plane insulation between the coil and support cylinder, and turn–to–turn insulation.

- The ground plane insulation must operate at relatively high voltages during quench conditions and will be subjected to strict QA controls. The design of the quench protection systems is based on a maximum voltage to ground of $500\,\mathrm{V}$. The ground plane insulation will be made by a $0.8\,\mathrm{mm}$ layer of fiberglass cloth inserted between the support cylinder and the solenoid outer layer during the winding. Summing up

this insulation layer to the cable insulation we get a ground insulation of $\sim 1.\,\mathrm{mm}$ We are confident from the previous experience on similar solenoids (BaBaR, Zeus, CMS) that this ground insulation thickness should be adequate to withstands the quench voltage of $\sim 500\,\mathrm{V}$ The insulation will be fully tested at $2\,\mathrm{kV}$ along the winding process. At the end of the ground plane insulation will be fully vacuum impregnated with high strength epoxy resin.

- The conductor will be insulated with a double wrap of $0.125\,\mathrm{mm}$ glass tape during winding to give an insulation thickness of $0.2\,\mathrm{mm}$ (80% compacted). The resulting turn–to–turn insulation thickness will be $0.4\,\mathrm{mm}$ and will be fully impregnated in the bonding process. Electrical tests will be carried out during winding to detect any failure of insulation. The tests will include regular/continuous testing for turn–to–turn and turn–to–ground insulation.

4.3 Quench Protection and Stability

Protection Concept

The solenoid will be protected by an external dump resistor which will determine the current decay under quench conditions and allow extraction of 75% of the stored magnetic energy. The quench protection concept is shown in fig. 9, and quench parameters are given in table 6. The protection concept is based on two main criteria.

Since the calculated stored energy for the magnet is $\sim 20\,\mathrm{MJ}$ at an operating current of $5000\,\mathrm{A}$, an inductance of $1.6\,\mathrm{H}$ is expected. To have a sufficiently fast and effective quench spreading and energy extracion, a $0.1\,\Omega$ was chosen. The time constant of this circuit during a fast discharge is so $16\,\mathrm{s}$.

- A voltage limit of $500\,\mathrm{V}$ across the solenoid applies during fast discharge. Center-tapping of the fast dump resistor to ground will limit the voltage to ground to $250\,\mathrm{V}$. The center–tapped resistor will also allow the measurement of ground leakage currents as a safety and diagnostic tool.

- An upper temperature limit of $100\,\mathrm{K}$ applies during quench conditions. This limit will give very good safety margins against peak temperature rise and thermally induced stresses at quench.

Quench Analysis

A preliminary quench analysis of the $\bar{\mathrm{P}}\mathrm{ANDA}$ solenoid has been made using a code developed for indirectelly cooled solenoid design. The code models the thermal and inductive behavior of the solenoid in order to account for quench–back effects and heat

Parameter	Value
Winding:	
ID	$2090\,\mathrm{mm}$
OD	$2190\,\mathrm{mm}$
Length	$2695\,\mathrm{mm}$
Weight	$2.0\,\mathrm{t}$
Supporting Cylinder:	
Material	Al alloy 5083
ID	$2190\,\mathrm{mm}$
OD	$2290\,\mathrm{mm}$
Length	$2775\,\mathrm{mm}$
Weight	$3.1\,\mathrm{t}$
Ground Insulation:	
Material	Fiberglass epoxy
Thickness	$0.8\,\mathrm{mm}$
Total Solenoid Weight:	$5.1\,\mathrm{t}$
Nuclear Interaction Length:	
(Assuming Aluminum)	
Maximum	$0.2\,\lambda_{\mathrm{int}}$
Minimum	$0.15\,\lambda_{\mathrm{int}}$

Table 5: Cold mass ($4.5\,\mathrm{K}$) parameters.

transfer to the support cylinder. This analysis shows that quench–back is predicted about two seconds after opening the protection circuit breakers.

Several different calculations were performed (courtesy AS-G Superconductors, formerly known as Ansaldo superconductors), simulating a local temperature rise in different locations on the coil. It was seen that the worst situation is encountered when he quench is generated in the downstream, internal coil. The temperature of the various windings[1] are reported in fig. 10: never in any simulation the temperature on the superconducting cable exceeded $65\,\mathrm{K}$, and in every situation the temperature, after a short period, drops to $\sim 40\,\mathrm{k}$.

The role of the coil former as a quench spreader has been studied comparing the

[1]The coils are numbered this way: 1. external upstream; 2. external central; 3. external downstream; 4. internal downstream; 5. internal central; 6. internal upstream.

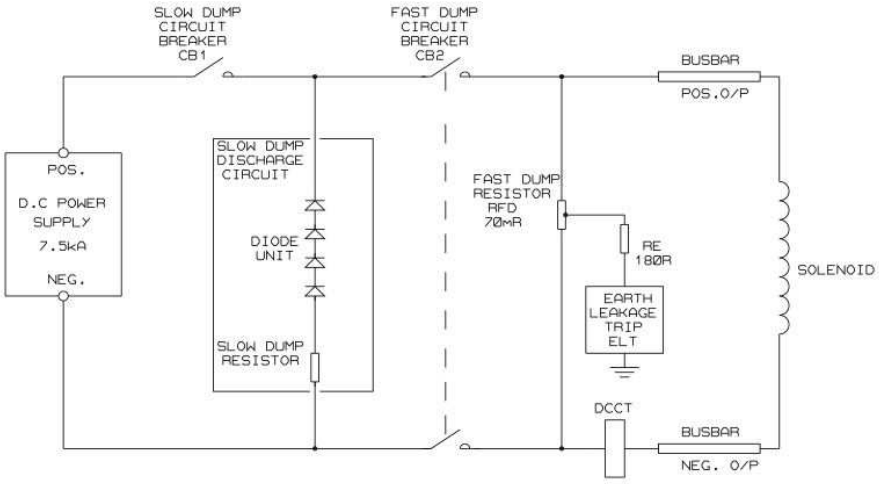

Figure 9: Solenoid power and and quench protection concept.

temperature rise with and without the coil former itself: this case is similar to the one of a coil former made of a poor heat and current conductor, such as stainless steel, carbon fibre or similar. Even in this configuration, the quench remains limited to the coil in which is started and in the closest one, and the temperature doesn't exceeds $80\,\mathrm{K}$.

Fig. 11 shows the voltage a the ends of each winding and the current in the coil after a quench: a time constant of $\sim 16\,\mathrm{s}$ is otbained, confrming the value of inductance of $\sim 1.6\,\mathrm{H}$ obtained from pure magnetic calculations.

Stability

The $\bar{\mathrm{P}}\mathrm{ANDA}$ solenoid coil will be indirectly cooled using the technology established for existing detector magnets such as DELPHI and ALEPH. The reliable operation of those magnets has demonstrated that safe stability margins can be achieved using high–purity, aluminum–clad superconductors in a fully bonded, indirectly cooled coil structure.

Conductor stability has been estimated using an analysis code in order to establish the minimum quench energy (MQE) for transient heat pulses. The computed $MQE = 1.4\,\mathrm{J}$. The computed minimum quench length (MQZ) is $0.6\,\mathrm{m}$.

These margins are considered to be safe for the $\bar{\mathrm{P}}\mathrm{ANDA}$ solenoid due to its low–stress design. The stability margin will be optimized during the full design study.

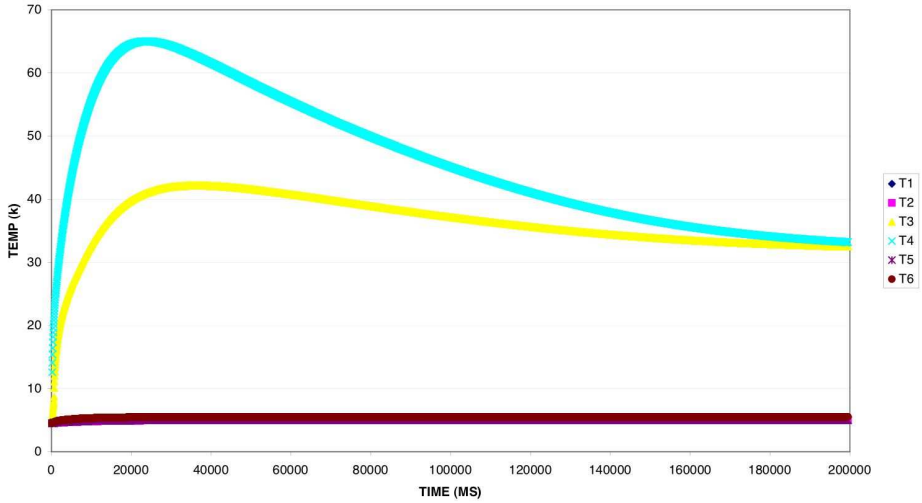

Figure 10: Temperature after a quench as a function of time for the 6 windings in the worst situation (courtesy AS-G Superconductors).

4.4 Cold Mass Cooling

Cooldown

Cold mass cooldown is accomplished by circulating cold helium gas either directly from the refrigerator or from a storage dewar with gas mixing.

Operating Conditions

Under operating conditions, the cold mass is cooled by circulating two–phase helium in pipelines welded on the coil support cylinder. The cooling circuit will be driven either by forced or natural (thermo–syphon) convection. This technology is established and yields the simplest operational mode. The thermo–syphon cooling circuit is designed for high flow rates to ensure the correct quality factor for the helium. The circuit is fed through a manifold at the bottom of the support cylinder. The cooling circuits are welded to the support cylinder surface with a spacing of $\sim 0.3\,\mathrm{m}$ to limit the temperature rise. The cooling pipes terminate in an upper manifold. The circuit will be designed to provide operation during quench conditions. In order to confirm these assumptions, a finite element model of 1/8 (thanks to the axial symmetry) of the coil–barrel has been developed. With the estimated static heat loads (reported in the next paragraph), a pipe diameter equal to $20\,\mathrm{mm}$ and a liquid helium mass flow of $28\,\mathrm{g/s}$, the maximum temperature rise is equal to $0.31\,\mathrm{K}$ with reference to the design temperature of $4.5\,\mathrm{K}$ (see Fig. 13). The conceptual layout of the cold mass cooling circuit (forced convection solution) is shown in fig. 12.

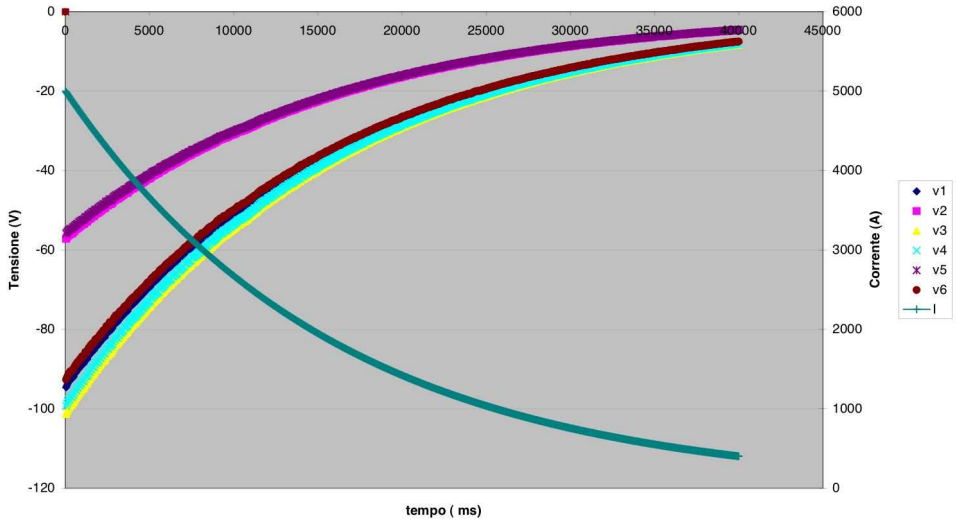

Figure 11: Voltage and current after a quench as a function of time for the 6 windings (courtesy AS-G Superconductors).

Heat Loads.

The estimated static heat loads for the solenoid are given in table 5. Eddy current heating in the support cylinder will cause additional heat loads during charging of the solenoid. However, for a solenoid charging time of $30\,\mathrm{min}$, the estimated transient power is $8\,\mathrm{W}$, which is small compared to static heat loads.

4.5 Cryostat Design.

Vacuum Vessel.

The cryostat consists of an annular vacuum vessel equipped with radiation shields and superinsulation. The vacuum vessel is designed to satisfy a number of basic criteria:

1. Support vacuum loads in accordance with recognized pressure vessel codes;
2. Carry the cold mass and radiation shield weight through the insulating supports;
3. Support magnetic loads (107 metric tons of axial forces) during nominal operations;
4. Operate with deflections of less than 1 mm under all loads when mounted in the flux return barrel;
5. Carry the weight of the inner detectors (The calorimeter actual weight is 18 metric tons. The calculation has been made with a magnifying factor of 1.15);

Parameter	Value
Operating Current	$5000\,\mathrm{A}$
Stored Energy	$20\,\mathrm{MJ}$
Inductance	$1.6\,\mathrm{H}$
Quench Voltage	$500\,\mathrm{V}$
Protection Resistor	$0.1\,\Omega$
Time Constant	$\sim 15\,\mathrm{s}$
Adiabatic Peak Temperature	$100\,\mathrm{K}$
Overall Current Density: Conductor 1	$54\,\mathrm{A/mm^2}$
Conductor 2	$36\,\mathrm{A/mm^2}$
Aluminum Stabilizer RRR Zero Field	1000

Table 6: Quench parameters

The vacuum vessel is designed as two concentric cylinders with thick annular end plates, all of aluminum alloy 5083; its basic parameters are given in table 8. The minimum thickness of the different parts composing the cryostat are calculated according to ASME Code for Pressure Vessels. A preliminary finite element (FE) structural analysis of the vessel has confirmed that design criteria (1)÷(4) can be met with reasonable safety factors. Maximum vessel deflections are less than $1\,\mathrm{mm}$, and stress levels peak up to $70\,\mathrm{MPa}$ with all loads applied (see Fig. 14). The cryostat can also be made of AISI 304 Stainless Steel; in this case, a decrease of deformability and an increase of stress level is expected.

Thermal Shielding. The cryostat is equipped with radiation shields, which operate at 40–80 K, and superinsulation. The shields are cooled by helium gas supplied directly from the refrigerator. About 30 layers of superinsulation separate the vacuum vessel walls from the radiation shields. Another five layers will be installed between the shields.

Services. Cryogenic supplies and current supplies are connected from a services turret to the cryostat through the service chimney in the backward end door. Current leads and local control valves are mounted in the services turret.

We foresee to use standard copper counterflow cryogenic current leads rated to the running current of the magnet: this means a LHe consumption of $17\,\mathrm{l/h}$. Cryogenic relief valves are also mounted in the service turret for quench and refrigeration failure conditions.

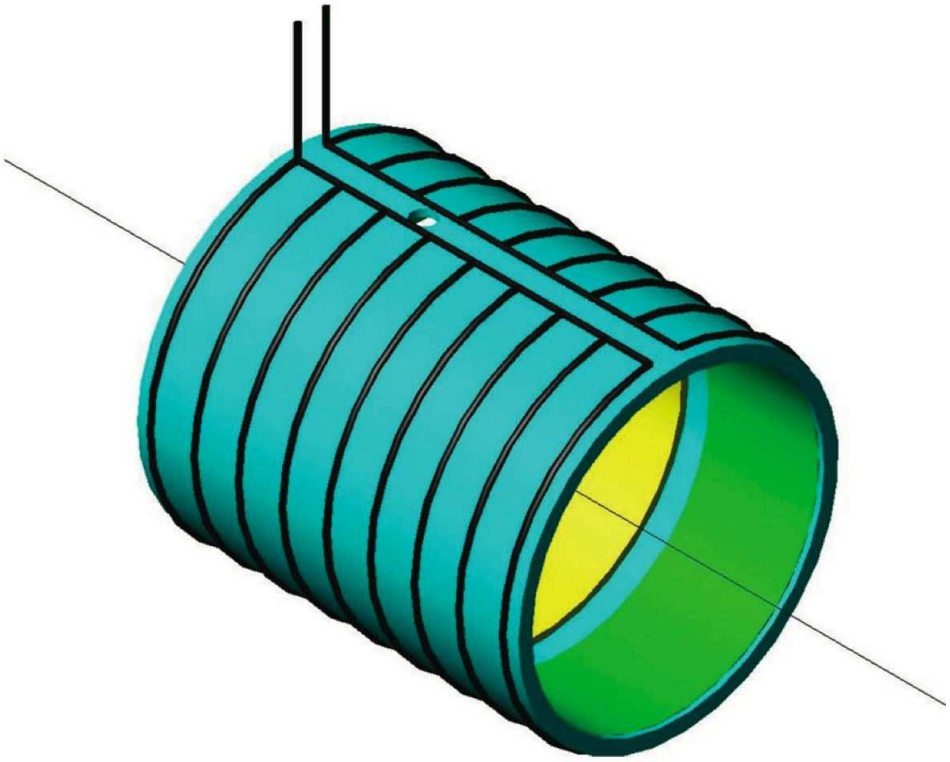

Figure 12: Cold mass cooling circuit. The cryogenic supply chimney passes through a cutout in the backward end of the barrel flux return.

4.6 Coil Assembly and Transportation.

The coil will be assembled inside the cryostat at the manufacturer's plant. Electrical and cryogen connections will be made at the chimney so that the coil can be tested before shipping.

A complete cooldown will be carried out from room temperature to the operating temperature of $4.5\,\mathrm{K}$. The cooldown will allow checking of cooling time, temperature control, heat loads, and full operation of sensors. A magnetic test will also be performed at low field (30% of the operating current) to check superconductor operation, the joint resistance, and the additional losses due to the eddy currents in the outer structural cylinder at the coil ramp-up.

Before delivering the magnet, but after the tests at the factory, the end flanges will be dismounted to allow a hard connection of the cold mass to the cryostat walls. Depending on the transport facilities, the cryogenic chimney may also be dismounted. In this case, the electrical and cryogen connections also must be dismounted and protected against

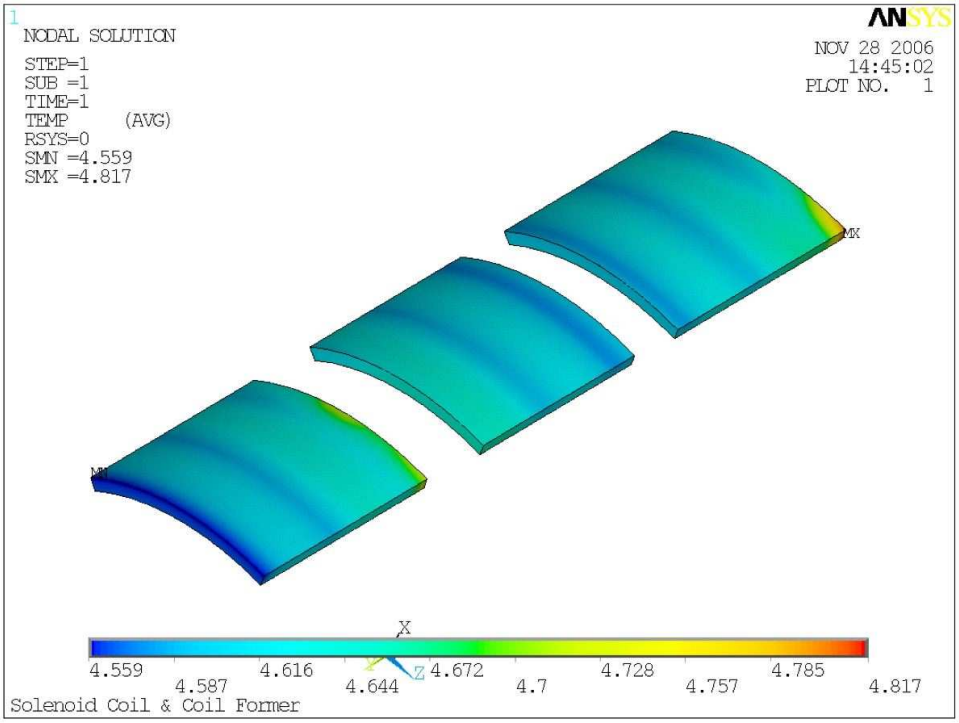

Figure 13: Cold mass cooling circuit. Temperature distribution in one eight of the assembly - nominal condition.

breakage.

5 Cryogenic Supply System and Instrumentation.

Operation of the superconducting solenoid requires both liquid helium and cold helium gas ($20\,\mathrm{K} \rightarrow 100\,\mathrm{K}$) for cooldown and refrigeration of the thermal shields. Similar systems have been used successfully throughout the HEP community. A summary of the cryogenic loads is given in Table 7.

The solenoid is equipped with a full set of instrumentation sensors for monitoring, control, and diagnostic purposes. Instrumentation includes temperature sensors for the cold mass, shield cryogen flow monitoring, and strain gauges in the coil support cylinder. Voltage taps monitor the electrical resistance of the conductor joints and quench detection. The quench detection systems are hardwired to interlocks. The solenoid instrumentation and controls are integrated with the BABAR experiment and refrigeration controls.

The liquid helium plant, which is fully automatic, is furnished with a process control system and all requisite logic and software necessary for all operational modes. Control

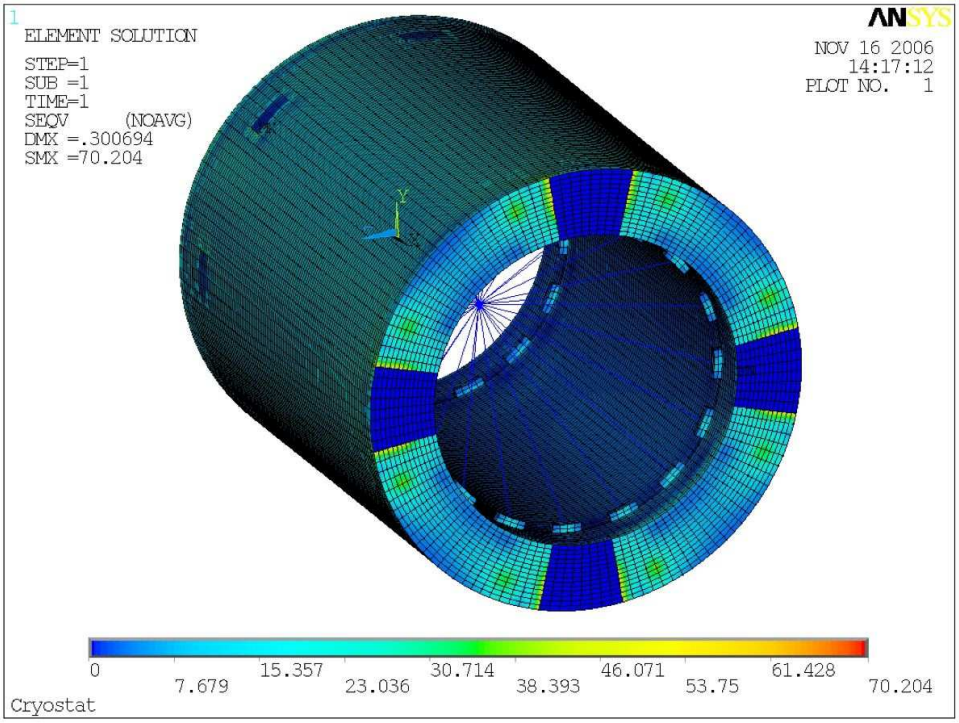

Figure 14: Vacuum Vessel FEM model, equivalent stress with all loads applied.

and monitoring of the cryogenic plant and the magnet coil, together with remote control and monitoring of the compressor room, is carried out from a control room adjacent to the plant room. Main operating parameters are interfaced with the $\bar{\mathrm{P}}$ANDA data acquisition and monitoring systems.

6 Flux Return.

6.1 Overview.

The flux return assembly provides the external flux path for the magnetic field from the superconducting solenoid. The flux return also provides the gravitational and seismic load path for the barrel detector components to the concrete foundation.

The flux return assembly consists of a barrel, four external support legs, two sets of end doors, roller mechanisms, and vertical adjustment systems. The design of the flux return and its components reflects the limitations of the experimental hall.

End door components must be movable once the detector is assembled to allow maintenance access to inner detector subsystems. The design of the flux return provides

Magnet Heat Loads at 4.2K	
Item Parameter	Load
Cold Mass	$5000\,\mathrm{kg}$
Total Surface Area	$44\,\mathrm{m}^2$
Radiation Heat Flux (Design)	$0.07\,\mathrm{W/m}^2$
Radiation Heat Load (Design)	$3.1\,\mathrm{W}$
Conduction Heat Load	$2.2\,\mathrm{W}$
Cable Joints	max $2\,\mathrm{W}$
Cryogenic Chimney	$10\,\mathrm{W}$
Gas Load	$1\,\mathrm{W}$
Eddy Currents ($1500\,\mathrm{s}$ ramp time)	$10\,\mathrm{W}$
Total $4.5\,\mathrm{K}$ (SF of 2)	$57\,\mathrm{W}$

Magnet Shield Heat Loads at 60K	
Item Parameter	Load
Shield Mass	$1000\,\mathrm{kg}$
Total Surface Area	$44\,\mathrm{m}^2$
Radiation Heat Flux (Design)	$1.3\,\mathrm{W/m}^2$
Radiation Heat Load (Design)	$57\,\mathrm{W}$
Conduction Through Supports	$17\,\mathrm{W}$
Conduction To Shields[2]	$150\,\mathrm{W}$
Diagnostic Wires	$1\,\mathrm{W}$
Gas Load	$2\,\mathrm{W}$
Eddy Currents ($1500\,\mathrm{s}$ ramp time)	$10\,\mathrm{W}$
Total $60\,\mathrm{K}$	$237\,\mathrm{W}$

Table 7: Cryogenic heat loads.

a means for proper alignment of all flux return components with respect to the detector magnet and the beam line. This alignment must be reestablished after maintenance is performed.

Analysis of the Flux Return.

The flux return analysis will investigate the overall structural integrity, including that of the supporting structures. This includes looking at all the components and connections involved in the operation, assembly, and seismic loadings of the structure. Operating loads for the barrel include both the gravitational and the magnetic forces. Assembly loads include any additional fixture weights that need to be attached during assembly.

Envelope Dimensions	
Inner Radius	$950\,\mathrm{mm}$
Outer Radius	$1340\,\mathrm{mm}$
Length	$3100\,\mathrm{mm}$
Inner Cylinder Thickness	$10\,\mathrm{mm}$
Outer Cylinder Thickness	$30\,\mathrm{mm}$
Annular End Plates Thickness	$50\,\mathrm{mm}$
Materials	AL5083, AISI 304

Design Loads	
Vessel Weight	$6\,\mathrm{t}$
Cold Mass	$5\,\mathrm{t}$
Calorimeter	$18\,\mathrm{t}$
Other Detectors	$3\,\mathrm{t}$

Table 8: Vacuum vessel parameters.

6.2 Barrel Flux Return Description.

The barrel flux return assembly extends $4050\,\mathrm{mm}$ in z, and the center is positioned $650\,\mathrm{mm}$ from the interaction point in the positive z direction. The barrel flux return extends radially from the detector axis from $1440\,\mathrm{mm}$ to $1840\,\mathrm{mm}$ and consists of 8 equal sectors that form an octagonal shape. The sectors consist of blocks with multiple steel plates oriented parallel to the axis of the solenoid.

The inner and outer parallel plates of each block are welded into a rigid superlayer using full penetration welds along their entire thickness in the radial direction (perpendicular to the beam line). The sectors are kept in place with a system of welds and supports that makes the whole barrel sufficiently rigid to keep all the magnetic and gravitational forces. The structure foreseen to host the muon chambers si mounted independently with the same technique.

The use of double block construction for each of the octagonal sectors of the barrel flux return ins't sufficient to provide a significant safety margin with respect to the $25\,\mathrm{t}$ rated capacity of the overhead crane in experimental hall. To mount the barrel, a dedicated machinery from the outside will be used. The weight of the barrel flux return is $180\,\mathrm{t}$ excluding the external support legs.

Muon chambers structure.

In downstream direction several layers of muon detectors are foreseen. The first double–layer will be mounted between the outer surface of the cryostat and the inner

surface of the barrel, starting at $z = 750\,\mathrm{mm}$ w.r.t. the interaction point. The presence of this element is needed to achieve a rough tracking of low energy muons: on the other hand, this imposes a gap between the cryostat and the barrel and so additional radial supports are needed.

An "E" structure is foreseen outside the barrel, made of the same steel of the barrel itself, to contain two single–layer muon detectors see fig. 15). Another double–layer will be mounted outside this structure. The steel act as a stopper for the muons and the magnetic field causes a deflection of the tacks, so a certain energy sensitivity can be achieved even with a so small number of active elements.

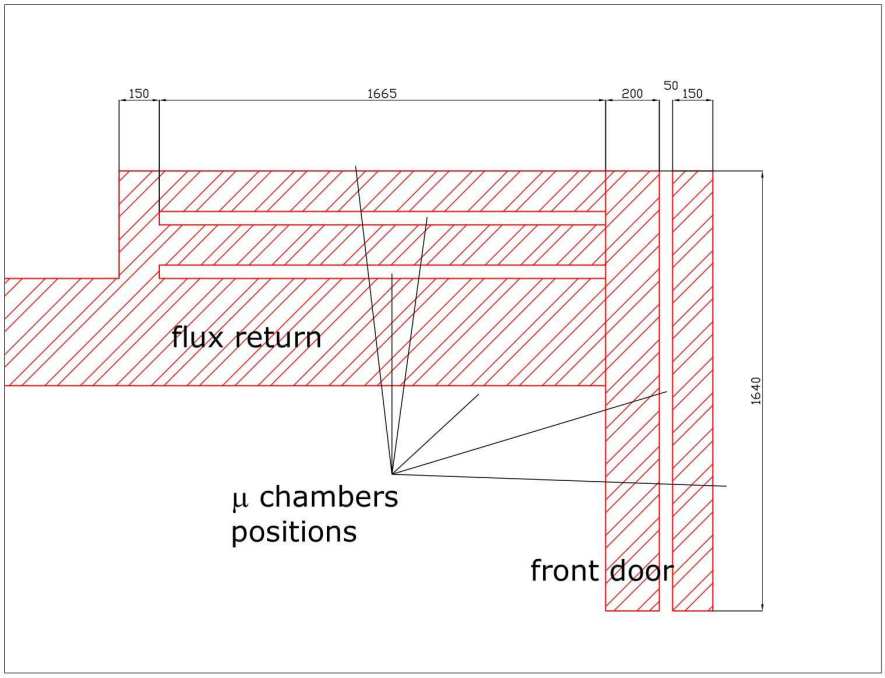

Figure 15: Particular of the muon housings in the flux return yoke.

External Support Legs.

Two external support leg assemblies provide the gravitational and seismic load path from the barrel flux return to the concrete foundation. Each assembly consists of two legs positioned $3200\,\mathrm{mm}$ apart in z. The legs are fabricated from $30\,\mathrm{mm}$-thick structural steel plates.

Included at each support leg is a $100\,\mathrm{t}$ capacity roller and a $150\,\mathrm{t}$ capacity jack.A preformed fabric pad is positioned between the jack and the roller to add compliance to the

system. The horizontal spacing of the jack and roller assemblies is nominally $5000\,\mathrm{mm}$. Each support leg is approximately $2750\,\mathrm{mm}$ in length, $1400\,\mathrm{mm}$ in width, and $2000\,\mathrm{mm}$ in height. The weight of each support leg assembly is approximately $20\,\mathrm{t}$.

6.3 End Door Description.

The forward and backward end doors are an array of steel plates that form a regular octagon with a central round hole. Both in upstream and downstream direction the end caps are vertically divided in two halves and can be open to let people operate inside the barrel.

Each end door is mounted on a skid that permits it to be raised onto high load capacity rollers by hydraulic jacks and to be moved on tracks located in the experimental hall. This provides a means to move the end doors into proper alignment with the barrel prior to being bolted in place, and to be moved away from the barrel for maintenance access to the detector. The center of gravity of the end door plates is high compared to the depth of the base. The skid provides additional stability during the horizontal accelerations experienced during moving or seismic events.

During operation, the magnet exerts an inward axial force that causes a significant bending moment on the end door plates. The downstream end doors also support the weight of the shielding screen of the dipole magnet and carry the axial magnetic load induced in the plug. To resist gravitational and seismic loads, and to limit the plate stresses and deflections, all the end door plates are joined together to form a single structural member.

The design of the end doors permits each door to be assembled and disassembled inside the experimental hall with the existing facility crane. Each end door is therefore composed of two weldments that are fastened together at installation. The inner weldment consists of four $50\,\mathrm{mm}$ plates, with each plate welded to a channel–shaped frame that extends along the top and bottom of the octagon shape and along the boundary between the right and left doors. Additional stiffeners are required to stiffen the weldment and help maintain the necessary gap for the muon chambers. The outer weldment consists of three $50\,\mathrm{mm}$ plates welded together with similar stiffening members. The detailed analysis of the response of the plates to the magnetic force distribution is not yet available, nor has a detailed seismic analysis been done for the end door plates. Several design options are being studied that can provide the necessary strength and stiffness.

The inner and outer weldments are joined together at installation by bolting each weldment to the top of the skid along the bottom of the octagon, and by bolting tie plates around the remaining perimeter of the weldments, except where the shielding plugs are

located. The outside tie plates are bolted in place after the muon chambers are installed, and provisions for cabling are provided in these outside plates. These tie plates are also used to attach the end doors to the barrel of the flux return.

In upstream direction, the diameter of the hole is fixed by the radius of the DIRC used for PID: its design radius is $550 \div 600\,\mathrm{mm}$, so the hole radius is $700\,\mathrm{mm}$, in order to house the trimming coil used to reduce the stray magnetic field in the DIRC PMT region. The end cap has an octagonal shape and fits the dimensions of the return flux barrel: the distance between two sides is $3680\,\mathrm{mm}$. The gap between the two weldments is left vacant (except for stiffeners): the outer weldment roles as a clamp for the fringe field which cannot be brought by the inner one.

In downstream direction the diameter of the hole is fixed by the geometrical acceptance of the detector: since the dipole part of the detector is intended to cover an angle of 10° around the beam axis, an opening of $600\,\mathrm{mm}$ is needed to let particles exiting at small angles get out of the flux return. The distance between two far sides of the octagon is $4480\,\mathrm{mm}$. The gap between the two weldments hosts a single–layer of muon chambers and a double–layer is foreseen just out of the outer weldment.

End Door Skids.

Each end door is mounted on a skid that is equipped with four $70\,\mathrm{t}$ capacity rollers, and four $45\,\mathrm{t}$ hydraulic jacks, one in each corner, which allow each of the doors to be moved relative to the barrel for maintenance access. The rollers ride on hardened steel tracks that are permanently located in the floor of $\bar{\mathrm{P}}\mathrm{ANDA}$ hall.

The end doors are bolted either to the barrel of the flux return when in the operating position or to seismic restraint brackets when in the parked position. While the doors are being moved, the $30\,\mathrm{t}$ counter weight provides lateral stability for a horizontal acceleration of $0.3\,\mathrm{g}$.

6.4 Options and Detailed Design Issues.

A detailed stress and deflection analysis is proceeding for the finalized overall envelope dimensions. A detailed magnetic field and force analysis of the end doors ensures that they will have adequate strength and stiffness to meet all the requirements imposed on them. The tolerance on plate flatness must be defined together with the envelope dimensions of the Muon Chambers. Standard mill tolerances for plate flatness do not meet our requirements for the end door plates to permit reliable MC installation; these tolerances exceed $15\,\mathrm{mm}$, half the nominal gap width. This issue, together with weld distortion in the plates during fabrication, must be resolved with both the plate supplier and the barrel and end door fabricator. Other manufacturing tolerances must be established as the

system interface dimensions are finalized.

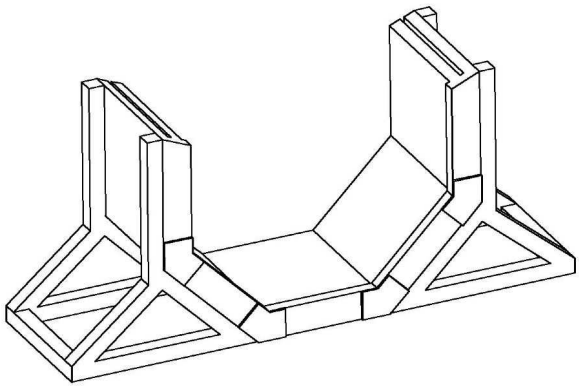

Figure 16: Step 1 - Outer base plates placement on back support structure

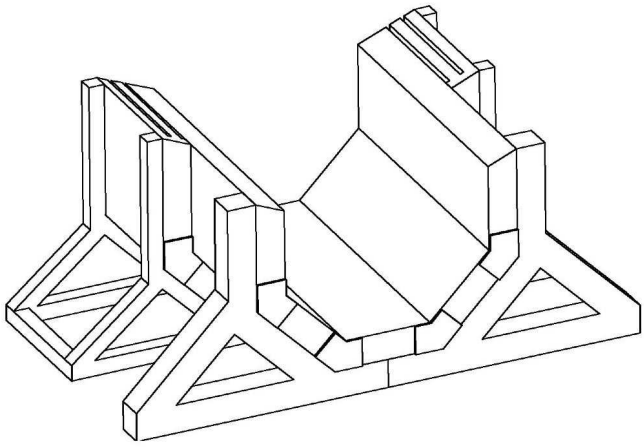

Figure 17: Step 2 - Inner lateral plates placement on support structure

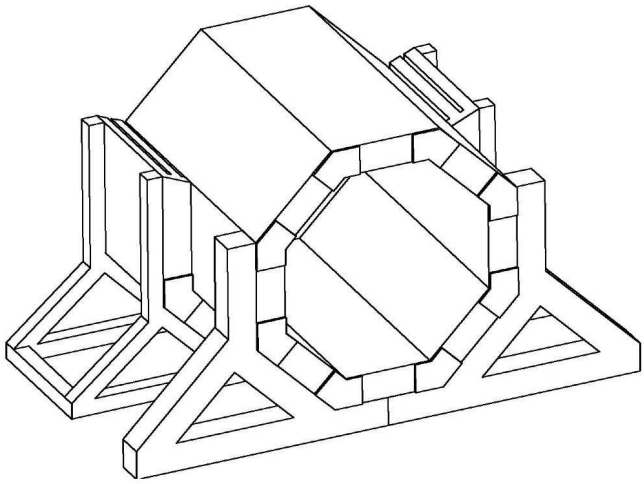

Figure 18: Step 3 - Inner top plates placement on lateral plates (an internal support stand is recommended)

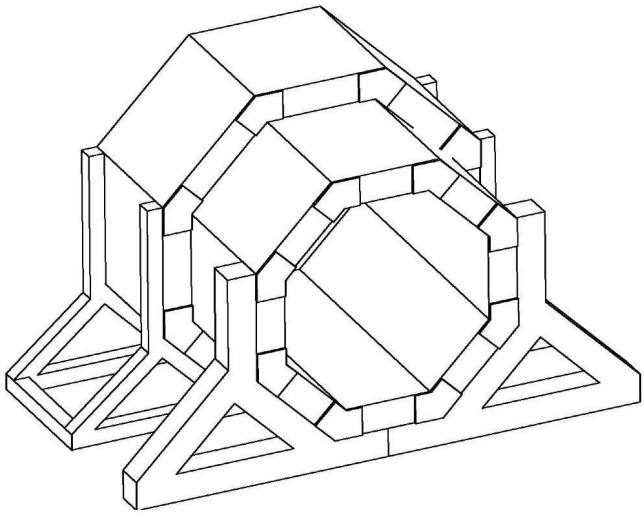

Figure 19: Step 4 - Outer top plates placement on inner top plates

6.5 Procurement, Fabrication, Assembly, and Schedule.

The barrel and the end doors will be built by the same fabricator as part of the same procurement contract. This will eliminate some duplication in the review of vendor qualifications, quality control plans and actions, and many contract administration issues. In addition, control of other characteristics of the plate material, such as the chemistry of the plates as it affects weldability and machinability, the mechanical properties of the plate, etc., may be more easily tracked by having one set of acceptance inspection criteria from one supplier for all plates.

The barrel and end doors will be fully assembled and inspected at the fabricator's shop. In this way, any problems that arise can be solved before final assembly in the $\bar{\mathrm{P}}$ANDA hall. This will also permit a thorough review of the assembly procedure by an experienced fabricator and ensure that the necessary lifting and assembly fixtures are functional and are provided with the barrel and end doors. The details of the fabrication and assembly plan will be developed by the fabricator subject to the review of the responsible design engineer in the $\bar{\mathrm{P}}$ANDA collaboration. A proposal for the assembly sequence is provided in Figures 16 to 19.

7 Acknowledgments

This work was realized thanks to the valuable contribution of AS-G Superconductors, especially thanks to Nicolò Valle and Matteo Tassisto; another important help came from Pasquale Fabbricatore, from INFN Genova.

We thanks also the technical experts from GSI, especially Bernd Lewandowski, for the fruitful collaboration, and Inti Lehmann, on behalf of the Glasgow group.

This work has been partly supported by the EU FP6 under the "DIRAC secondary beam" project, contract N. 515873.

References

[1] PANDA Collaboration, Technical Progress Report (2005)
K. T. Brinkmann, P. Gianotti and I. Lehmann, Nucl. Phys. **NEWS16** (2006) 15 [arXiv:physics/0701090].

[2] H. Desportes et al., "Construction and Test of the CELLO Thin–Wall Solenoid," **Ad. Cryogenics Eng. 25**, 175 (1980).

[3] ASME, "1992 ASME Boiler and Pressure Vessel Code" (1992).

[4] EuroCode3, “Design of steel structures”, **EN-1993**.

[5] CNR, “Costruzioni di acciaio. Istruzioni per il calcolo, l’esecuzione, il collaudo e la manutenzione”, **CNR 10011/97** (1997).

[6] ANSYS INC, “General Finite Element Code,” Rev. 10.0 (2005).

[7] M.S. Lubell, “Empirical scaling formulas for critical current and critical field for commercial NbTi”, **IEEE Trans on Mag MAG-19**, 720 (1983).

[8] D. Andrews et al., “A Superconducting Solenoid for Colliding Beam Experiments,” **Ad. Cryogenic Eng. 27** (1982).

[9] E. Baynham and P. Fabbricatore, “Superconducting Solenoid for the BABAR Detector,” **BABAR TDR**.

[10] A. Bonito Oliva et al., “ZEUS Magnets Construction Status Report,” 11th Int. Conference on Magnet Technology, **MT–11**, 229 (1989).

[11] P. Clee et al., “Towards the Realization of Two 1.2 T Superconducting Solenoids for Particle Physics Experiments,” 11th Int. Conference on Magnet Technology **MT–11**, 206 (1989).

[12] H. Desportes et al., “General Design and Conductor Study for the ALEPH Superconducting Solenoid,” **J. Phys. (Paris) C1–341**, (1984).

[13] Y. Doi et al., “A 3T Superconducting Magnet for the AMY Detector,” **Nucl. Instr. Methods A274**, 95 (1989).

[14] M.A. Green et al., “A Large Superconducting Thin Solenoid for the STAR Experiment at RHIC,” **IEEE Trans. App. Superconductivity**, 104 (1993).

[15] C.M. Monroe et al., “The CLEO–II Magnet–Design, Manufacture, and Tests,” **ICEC–12**, 773 (1988).

[16] M. Wake et al., “Excitation of a Superconducting Large Thin Solenoid Magnet,” **MAG–23**, 1236 (1987).

[17] F. Wittgenstein et al., “Construction of the L3 Magnet,” 11th International Conference on Magnet Technology, **MT–11**, 131, (1989).

[18] A. Yamamoto et al., “Thin Superconducting Solenoid Wound with the Internal Winding Method for Colliding Beam Experiments,” **J. Phys. (Paris) C1–337**, (1984).